J. Fluid Mech. (2004), *vol.* 498, *pp.* 205–225.
DOI: 10.1017/S0022112003006682 Printed in the United Kingdom

The role of inertia in extensional fall of a viscous drop

By Y. M. STOKES AND E. O. TUCK

Department of Applied Mathematics, University of Adelaide, Australia

(Received 6 September 2001 and in revised form 12 August 2003)

In flows of very viscous fluids, it is often justifiable to neglect inertia and solve the resulting creeping-flow or Stokes equations. For drops hanging beneath a fixed wall and extending under gravity from an initial rest state, an inevitable consequence of neglect of inertia and surface tension is that the drop formally becomes infinite in length at a finite crisis time, at which time the acceleration of the drop, which has been assumed small relative to gravity g, formally also becomes infinite. This is a physical impossibility, and the acceleration must in fact approach the (finite) free-fall value g. However, we verify here, by a full Navier–Stokes computation and also with a slender-drop approximation, that the crisis time is a good estimate of the time at which the bulk of the drop goes into free fall. We also show that the drop shape at the crisis time is a good approximation to the final shape of the freely falling drop, prior to smoothing by surface tension. Additionally, we verify that the drop has an initial acceleration of g, which quickly decreases as viscous forces in the drop become dominant during the early stages of fall.

1. Introduction

Extensional flow and break-off of viscous fluid drops has been much studied (see the review article by Eggers 1997 and articles cited in Stokes, Tuck & Schwartz 2000). In particular, fall under gravity of a drop of very viscous fluid hanging under a solid boundary, such as honey dripping from a spoon held upside-down, was examined by Stokes *et al.* (2000). Because of the high viscosity of the fluid and the relatively large lengthscale, both inertial and surface tension forces were assumed to be small relative to viscous and gravitational forces, and were therefore neglected in that study. The resulting creeping-flow problem was then solved using both a slender-drop approximation and exact finite-element computational methods. However, neglect of inertia in the latter stages of the fall of the drop, when its acceleration is no longer small and in reality must approach the free-fall value g, results in a finite 'crisis' time at which the length and acceleration of the drop formally become infinite, simultaneously with its cross-sectional area becoming zero at some point along its length (often close to the solid boundary).

Wilson (1988) suggested for a similar problem that this non-physical infinity could be removed by putting inertia back into the problem, and also identified the crisis time with the time at which the drop breaks. Kaye (1991) considered some problems of viscous extensional flow both with and without inertia, and Cram (1984) included inertia in a numerical study of falling drops, but neither discussed the effect of inertia on the crisis time or acceleration. More recent references on drops that are falling

and/or in extensional flow include Henderson *et al.* (2000), Wilkes, Phillips & Basaran (1999) and Sarkar & Schowalter (2001).

Clearly, inertia can only be justifiably neglected when the acceleration of the fluid in the drop is small compared to the acceleration due to g, and inclusion of inertia terms in the equations of motion should lead to a solution that agrees more closely with reality in circumstances where this assumption breaks down. It is of interest to demonstrate this explicitly, and so determine the time at which inertia begins to play a significant role, in the latter stages of the fall of the drop.

Actually, inertia must also be important in the very earliest stages of its fall. Neglect of inertia yields Stokes-flow equations which imply that the initial instantaneous acceleration of the drop is infinite and that the drop starts with an impulsively developed initial velocity. In practice, it must undergo an acceleration from rest of magnitude g, which is large compared to the fluid accelerations that apply soon after motion begins, when viscous retarding forces in the drop are dominant. Again the physics requires inclusion of inertia in any analysis of the very early stages of the flow, if we wish to estimate the true magnitude of the accelerations.

We emphasize here the role of inertia in extensional flow and drop formation, while in the present study still neglecting surface tension. This neglect of surface tension does demand justification, especially since surface tension is usually believed to be of primary importance immediately before and during the final drop pinch-off. A comparison of the relevant scales in this class of problem shows that surface tension becomes important when the gravitational Bond number

$$Bo = \frac{\rho g \ell^2}{\gamma}$$

(based on an appropriate length scale ℓ such as the mean drop diameter, where γ is surface tension and ρ is density) is of order one or smaller. In physical terms, this simply states that surface tension is important when such lengths ℓ are comparable to or smaller than the meniscus size $\sqrt{\gamma/(\rho g)}$, which for most fluids (including water, honey and molten glass) is about 2 mm.

In neglecting surface tension we thus focus our attention on development and fall of drops that are significantly larger in overall size than 2 mm, such as are typical for spoonfuls of honey, in metal arc welding with globular transfer, and in 'gob' formation in the glass moulding industry. Droplet diameters for globular transfer in welding may be 4 mm and larger (Haidar & Lowke 1996), while glass gobs may range from around 8 mm in diameter for production of optical glass elements (Gearing 1999) up to more than 100 mm, and weighing 30 to 50 kilograms, for production of CRT television bulbs (Kary *et al.* 2000).

An interesting geological application for large-drop research is the formation of salt domes (or diapirs), having diameters measured in kilometres and formed by buoyancy- and/or tectonic-driven viscous flow of salts in the earths crust. Large hydrocarbon reserves are sometimes associated with these structures and determining their shape is, therefore, of considerable interest to the petroleum industry (Barnichon *et al.* 1999).

In addition to relatively large drop size, we are also mainly concerned with the relatively long time period during which the main drop is evolving, before instability of very thin filaments and other small-scale phenomena demand inclusion of surface tension. Nevertheless, this theory predicts the formation of such thin filaments.

In the context of inertial influence on this extensional flow, the actual shape of the evolving drop is of considerable interest. The drop's shape as a function of time

is non-trivially and uniquely determined by its initial static shape, and only after a relatively long time in free fall will surface tension mandate smoothing of that shape, ultimately into a spherical drop. When inertia is neglected as in Stokes *et al.* (2000), we are able to compute a drop shape up to but not beyond the finite crisis time. However, since we anticipate break-off at close to this time, the drop shape at this crisis time should be a good approximation to the subsequent shape of the freely falling drop.

On the other hand, as soon as inertia is included in the analysis, the computations can proceed beyond the crisis time of the inertialess theory, into a regime where the main drop is nearly in free fall as if it were a rigid body, with an extending and thinning filament (which has a decreasing effect on its dynamics) connecting it to the wall. Then we can determine just how well the shape of this almost-rigid body compares with the drop shape at the crisis time predicted by the inertialess theory. In contrast to the inertialess theory, with inertia included and in the absence of surface tension, the connecting filament never formally breaks, but becomes ever longer and thinner as time increases.

As indicated above, eventually when the filament is sufficiently thin, surface tension can no longer be neglected but will play a significant role, ultimately causing the filament to break (Eggers 1993; Papageorgiou 1995). However, for very viscous fluids, such filaments can, in practice, persist for very long times, well beyond predictions given by current theories (Eggers 1997), becoming in the process very long and very much thinner than the meniscus length, as the simple household example of a drop of smooth honey readily shows. This behaviour is not yet well understood. It is, however, known that, near to breakup, a balance of viscous and surface tension forces alone is not sufficient to describe the evolution of the ever thinning thread and that inertia enters the dominant force balance (Eggers 1997; Renardy & Losh 2002). The present study which concentrates attention on the effect of inertia is a contribution to the understanding of highly viscous drops and filaments.

2. Mathematical formulation

We consider a drop of incompressible Newtonian fluid with density ρ and kinematic viscosity $\nu = \mu/\rho$, hanging beneath a horizontal surface at $x = 0$. The complete mathematical formulation is similar to that in Stokes *et al.* (2000), but with the addition of inertia. Thus, g acts in the x-direction and the Navier–Stokes and continuity equations are given by

$$\frac{\partial \boldsymbol{q}}{\partial t} + \boldsymbol{q}\cdot\nabla\boldsymbol{q} = g\boldsymbol{i} - \frac{1}{\rho}\nabla p + \nu\nabla^2\boldsymbol{q}\ , \tag{2.1}$$

and

$$\nabla\cdot\boldsymbol{q} = 0\ , \tag{2.2}$$

where $\boldsymbol{q}$ is the velocity vector, p is the pressure and $\boldsymbol{i}$ is the unit vector in the x-direction. We consider a drop that lies in $0 < x < L(t)$, where $x = 0$ is the wall boundary and $x = L(t)$ is the (to-be-determined) lower free end. The drop is assumed to be initially at rest with a given initial shape of radius $R_0(x, \theta)$ (using cylindrical polar coordinates) and having initial length $L_0 = L(0)$.

Equations (2.1) and (2.2) would usually be solved subject to no-slip boundary conditions at the wall $x = 0$ and zero-stress free-surface and kinematic conditions on all other boundaries, see Stokes *et al.* (2000). However, when using a zeroth-order slender-drop approximation, we must allow slip along the wall.

Once inertia is included in the analysis we need not be restricted to highly viscous fluids, but may measure the influence of inertia by a Reynolds number (see below)

$$Re = \frac{gL_0^3}{9\nu^2}\,. \tag{2.3}$$

For small Re, we expect the drop behaviour to be approximated well by the inertialess theory, with the quality of this approximation decreasing as Re increases. We present here a number of computed results enabling quantitative assessment of this effect. As already indicated, our main attention in the present paper is directed toward two matters, namely computation of the acceleration $L''(t)$ of the bottom point of the drop, and determination of the shape of the final freely falling drop. Very small Reynolds numbers Re will give the best comparison with results from the inertialess theory, but larger Reynolds numbers, i.e. less viscous fluids, display more clearly the large-time characteristics of a falling viscous fluid drop.

We provide here computations only for axisymmetric slender drops, although it is straightforward to treat similarly general three-dimensional drops or two-dimensional thin sheets. Hence, the drop has initial radius $R_0(x)$ and cross-section area $A_0(x) = \pi R_0^2(x)$ at station x, $0 \leqslant x \leqslant L_0$. Its subsequent shape is described by $R(x,t)$ or $A(x,t)$, $0 \leqslant x \leqslant L(t)$, where $R_0(x) = R(x,0)$ and $A_0(x) = A(x,0)$. In the absence of significant surface-tension effects, thin sheets and slender drops behave similarly, drop width in two dimensions being analogous to drop cross-section area in three dimensions. For extremely slender axisymmetric filaments, the large lateral curvature implies some surface tension effects which are absent in the equivalent two-dimensional case, but these effects do not have any major influence on the main-drop behaviour over the time frame of interest here. Rather they are of interest in the study of pinch-off and rupture of the filament to release the main drop into actual free fall. Significantly, our work (both here with inertia and previously in Stokes *et al.* (2000) without inertia), although neglecting surface tension, does give an indication of when and where the high-curvature factors causing filament rupture begin to become important, and hence when and where break-off of the drop is likely to occur, without specifying the surface-tension-dependent details of this subsequent event.

The full flow problem defined above may be solved without approximation, using finite elements, and we first do this to identify interesting features of the flow. Most (but not all) of these features are also captured by a semi-analytic slender-drop analysis to follow. An intuitive large-time asymptotic analysis for slender drops then gives an explicit formula connecting initial and final shapes, which is confirmed by the detailed computations.

3. Finite-element computations

A finite-element algorithm was described and used in Stokes *et al.* (2000) for computing the extension under gravity of a viscous drop, neglecting inertia. We need only modify this algorithm for the problem formulated above to include inertia.

First note that, because of the Lagrangian time-stepping method, the nonlinear nature of the inertia terms in the Navier–Stokes equations presents no difficulties. We simply discretize the acceleration $\mathrm{D}\boldsymbol{q}/\mathrm{D}t = \partial\boldsymbol{q}/\partial t + (\boldsymbol{q}\cdot\nabla)\boldsymbol{q}$ following a particle, using backward Euler differencing so that (2.1) becomes

$$\boldsymbol{q}^{n+1} - \Delta t\left(g\boldsymbol{i} - \frac{1}{\rho}\nabla p^{n+1} + \nu\nabla^2\boldsymbol{q}^{n+1}\right) = \boldsymbol{q}^n, \tag{3.1}$$

where Δt is the time-step size and $\boldsymbol{q}^n$ and p^n are the velocity and pressure distributions in the flow domain at the nth time step, with $\boldsymbol{q}^0 = \boldsymbol{0}$. The continuity equation (2.2) is just

$$\nabla \cdot \boldsymbol{q}^{n+1} = 0. \tag{3.2}$$

Now, let a fluid particle be labelled by its initial position vector $\boldsymbol{r}^0$, and let its position at time $t \geqslant 0$ be given by $\boldsymbol{r}(\boldsymbol{r}^0, t)$, with $\boldsymbol{r}(\boldsymbol{r}^0, 0) = \boldsymbol{r}^0$. In particular, $\xi = \boldsymbol{r}^0 \cdot \boldsymbol{i}$ is the initial x-wise distance of this particle below the wall. Then we compute the subsequent displacement of this particle by backward differencing, i.e.

$$\boldsymbol{q}^{n+1} = \frac{\mathrm{d}\boldsymbol{r}}{\mathrm{d}t}^{n+1} = \frac{\boldsymbol{r}^{n+1} - \boldsymbol{r}^n}{\Delta t}, \tag{3.3}$$

where $\boldsymbol{r}^n = \boldsymbol{r}(\boldsymbol{r}^0, n\Delta t)$ is the particle position at the nth time step. For a fixed time step Δt, displacements will become very large as time progresses and velocities increase, giving rise to numerical inaccuracy. Hence we set a maximum permissible displacement Δ_m for any fluid particle and decrease the time step as necessary to ensure that this is nowhere exceeded.

Thus, our computational algorithm can be summarized as follows:

(*a*) construct a mesh of interconnected nodes over the fluid region, each node representing a fluid particle;

(*b*) set $n = 0$;

(*c*) use the finite-element method to solve the discretized forms of the Navier–Stokes and continuity equations (3.1), (3.2) for the velocity $\boldsymbol{q}^{n+1}$ and pressure p^{n+1} at each of the mesh nodes, subject to the initial condition $\boldsymbol{q} = 0$ and no-slip and zero-stress conditions on the wall and free surface boundaries, respectively;

(*d*) determine the time step $\Delta t = \min(\Delta t, \Delta_m / |\boldsymbol{q}_i^{n+1}|)$ over all nodes i;

(*e*) solve (3.3) for the new position vector $\boldsymbol{r}^{n+1}$ of each mesh node;

(*f*) move each node to its new position;

(*g*) increment n and repeat steps (*c*)–(*f*) to obtain the time-evolution of the drop.

At time step $n = 1, 2, \ldots$, we can compute the downward vertical component a^n of the fluid acceleration of a mesh node, i.e. of a fluid particle, by simple backward differencing,

$$a^n = \frac{u^n - u^{n-1}}{\Delta t}, \tag{3.4}$$

where $u^n = \boldsymbol{q}(\boldsymbol{r}^n, n\Delta t) \cdot \boldsymbol{i}$ is the x-component of the velocity of that particle at time step n. In particular, the vertical acceleration $L''(n\Delta t)$, $n = 1, 2, \ldots$, at the centre-bottom of the drop, is given by (3.4) for the particle with $\xi = L_0$. Close to $t = 0$, we use a very small time step, but progressively increase this at larger times.

This algorithm has been implemented in the finite-element package *Fastflo*, CSIRO (1999). An augmented-Lagrangian method was used to solve for velocity and pressure (CSIRO 1999, pp. 165–169). Eventually, the computations must cease because of excessive stretching of mesh elements, leading to numerical inaccuracy and ultimately failure.

As our main example in this paper, we use an initially paraboloidal drop, with scaled cross-section area

$$\frac{A_0(x)}{A_0(0)} = \left(\frac{R_0(x)}{R_0(0)}\right)^2 = 1 - \frac{x}{L_0}, \quad 0 \leqslant x \leqslant L_0, \tag{3.5}$$

having its maximum value $A_0(0)$ at the wall. Results for a drop of initial aspect ratio $\alpha_r = R_0(0)/L_0 = 0.1$, with Reynolds number ranging from very small $Re = 0.001$ to

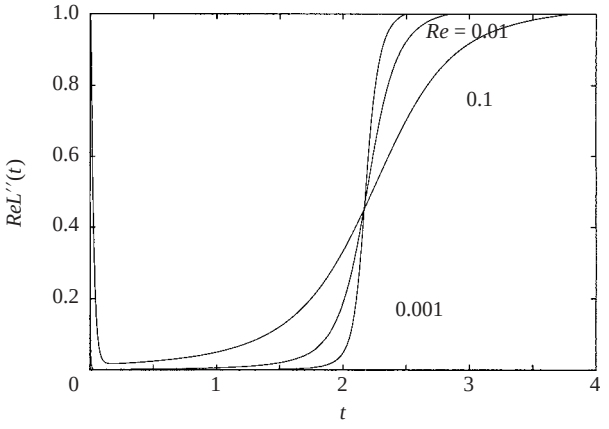

FIGURE 1. Scaled vertical acceleration at the bottom of the drop ReL'' versus scaled time t. Initially paraboloidal drop of aspect ratio $\alpha_r = 0.1$ at Reynolds numbers $Re = 0.001,\ 0.01,\ 0.1$.

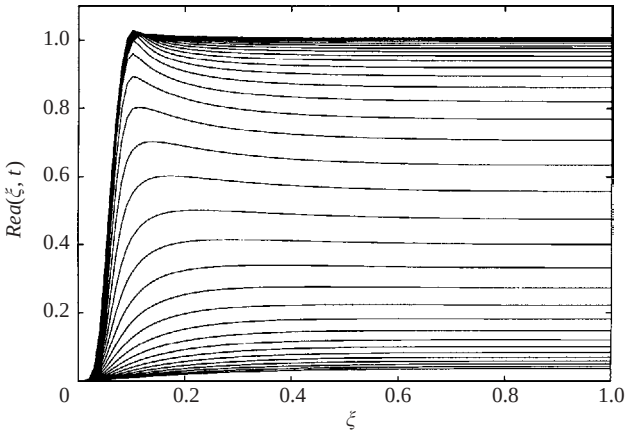

FIGURE 2. Acceleration along the drop centreline as a function of Lagrangian coordinate ξ, corresponding to initial distance from the wall. Initially paraboloidal drop of aspect ratio $\alpha_r = 0.1$ at Reynolds number $Re = 0.1$ and times $t = 0.8, 0.9, 1.0, \ldots, 4.0$.

somewhat larger $Re = 0.1$, are shown in figures 1 to 4. A mesh of 1027 quadratic triangular elements was used, with elements clustered near the wall where there is most distortion from the initial shape. Computations were continued at least until the drop acceleration had (very nearly) returned to g, but could not be taken too far beyond this time owing to excessive mesh distortion.

Results are presented in non-dimensional form using the length scale L_0, a time scale $T = \nu^*/(gL_0)$, and a velocity scale $U = gL_0^2/\nu^*$, where $\nu^* = 3\nu$ is the elongational kinematic viscosity (Bird *et al.* 1977, p. 30). This choice of viscosity and velocity and length scales corresponds to the definition (2.3) of the Reynolds number. The cross-section area $A(x, t)$ is scaled with $A_0(0)$ and the drop radius $R(x, t)$ is scaled with $R_0(0)$.

3.1. *Accelerations*

The scaled vertical acceleration $ReL''(t)$ of the bottom-most point of the drop, which is unity when the actual acceleration takes the value g, is plotted in figure 1. As

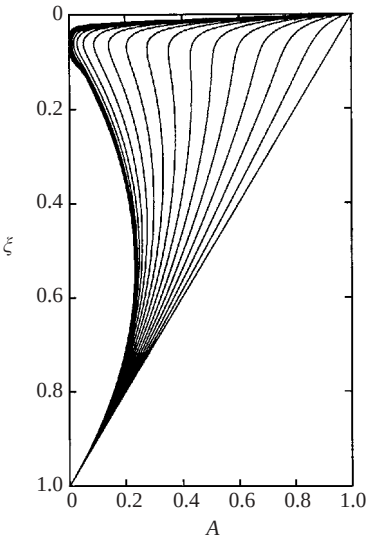

FIGURE 3. Lagrangian evolution of the initially paraboloidal drop of aspect ratio $\alpha_r = 0.1$ at Reynolds number $Re = 0.1$, i.e. scaled drop cross-section area A as a function of initial distance from the wall ξ, at times $t = 0.0, 0.2, 0.4, \ldots, 4.0$. The drop shape progressively changes from initially paraboloidal $A = 1-\xi$ to a final profile $A = (\xi - 0.7\alpha_r)(1-\xi)/(1-0.7\alpha_r)$, connected by a thin filament to the wall boundary at $\xi = 0$.

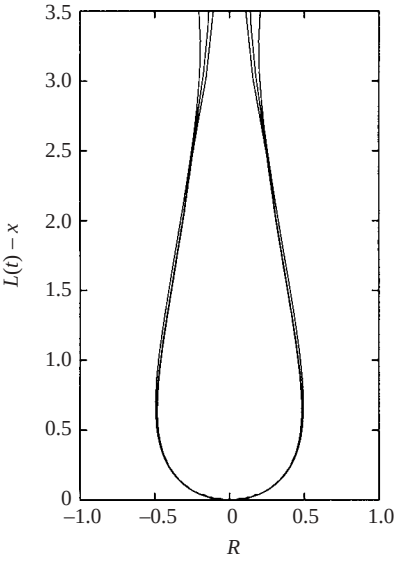

FIGURE 4. Eulerian drop shape, i.e. drop radius $R = \sqrt{A}$ as a function of distance $L(t) - x$ from the drop bottom, at $t = 2.5, 3.0, 4.0$, showing that the main drop is effectively a solid body at large time. Initially paraboloidal drop of aspect ratio $\alpha_r = 0.1$ at Reynolds number $Re = 0.1$.

expected, the actual acceleration starts at g, falls rapidly to a small value while viscosity dominates, and then rises, returning to g at large times when the drop is effectively in free fall. The smaller the Reynolds number, the faster and larger is the initial decrease in acceleration from g, the minimum actual acceleration being of

the order of Re times g. Further, the smaller the Reynolds number, the longer the acceleration remains small, but then the more rapid is the return to g, which also then occurs nearer to the crisis time of the inertialess theory, which is $t \approx 2$ for the present initially paraboloidal example, with $t \to 2$ as $\alpha_r \to 0$ (as seen later from (4.16)).

The above discussion relates strictly only to the acceleration of the particle at the very bottom of the drop. It is also of interest to consider other particles. Plotting vertical acceleration versus particle label ξ along the drop centreline, as is done for $Re = 0.1$ in figure 2, reveals an interesting characteristic of the flow in the falling drop.

In the very early stages of commencement of fall (not shown), the actual acceleration throughout most of the drop is g, but this acceleration quickly decreases in the viscosity-dominated time range. During this initial time, the curves show an acceleration increasing with ξ, with the maximum acceleration at the bottom $\xi = 1$.

However, this soon changes, and the particle with maximum acceleration soon becomes one that was initially close to the wall, with a label of the order of $\xi = \alpha_r \ll 1$, although in terms of the actual distance x, this particle is typically quite far from the wall for times $t > 0$. As this change occurs and as the acceleration throughout the lower bulk of the drop approaches g, the maximum acceleration in the upper part of the drop may even exceed g for some time. For the case $Re = 0.1$, $\alpha_r = 0.1$ illustrated in figure 2, the acceleration rises to a maximum value of about $1.03g$ when $t \approx 3.1$ and $\xi \approx 0.11$ ($x \approx 5.1$). Subsequently, the maximum acceleration decreases to g, until we effectively reach a steady state with the bulk of the drop in free fall. Decreasing the aspect ratio of the initial drop results in an increase in the peak value of acceleration (e.g. for $Re = 0.1$ and $\alpha_r = 0.05$, the acceleration reaches about $1.08g$ at $t \approx 2.8$), whereas decreasing the Reynolds number Re causes a decrease in this peak value, so that for $Re = 0.01$ and $\alpha_r = 0.1$ the acceleration in the drop does not significantly exceed g ever (to within numerical accuracy).

After a sufficiently long time, the fluid in a region just below the wall, of approximate initial scaled length α_r, has an acceleration that reduces rapidly from g at $\xi \approx \alpha_r$, to 0 at the wall $\xi = 0$. This region $0 < \xi < O(\alpha_r)$, occupying a smaller and smaller fraction of the initial length of the drop as the aspect ratio α_r decreases, includes but extends somewhat beyond the 'wall boundary layer' discussed in Stokes *et al.* (2000).

In figure 2 the acceleration profile reaches a steady state by $t \approx 4$. Reducing the Reynolds number reduces the time period during which the acceleration profile evolves, with this time period approaching a sudden jump at the crisis time $t \approx 2$ as $Re \to 0$ (cf. figure 1).

3.2. *Drop shapes*

In figure 3 we plot, for a range of times t and for $Re = 0.1$, the scaled drop cross-section area A versus the particle label ξ. This is a 'Lagrangian' evolution plot. Similarly, in figure 4 we plot a true Eulerian drop shape, namely R versus distance $L(t) - x$ from the bottom of the drop. The latter plot shows just the portion of the drop furthest from the wall containing the bulk of the fluid mass. Both plots show the drop shape to be effectively unchanging at large time, excepting for an ever-thinning filament connecting the main drop to the wall. Overall filament and drop shape R versus x is shown in figure 10.

At about $t = 3.1$, as the acceleration in the bulk of the drop nears g, there is a pinching of the drop near $\xi \approx \alpha_r$, corresponding to a particle located at a distance $L(t) - x \approx 3$ from the bottom of the drop and from where the filament extends back to the wall. The position and time at which this pinching becomes evident corresponds

to the position and time at which the acceleration in the drop reaches its maximum value. Referring to figure 2 we see that in the filament region above this position, the acceleration decreases to 0 at the wall, which is to be expected from physical considerations. Because this pinching occurs when the bulk of the drop has almost reached free fall, it will occur closer and closer to the crisis time as $Re \to 0$, and can be associated with the ultimate breaking off of the main drop.

The drop and filament behaviour can be understood with reference to the inertialess theory of Stokes *et al.* (2000). In the connecting filament attaching the drop to the wall, viscous forces are still dominant even at large times, so that the acceleration is small and inertia can therefore still be neglected in this region. The main bulk of the drop in virtual free fall below this filament exerts minimal force on the filament, so that we have, effectively, a thin fluid filament extending under the influence of its own mass alone. While the main drop shape remains fairly constant, the shape of the connecting filament will, in the absence of surface tension, develop according to the inertialess theory of Stokes *et al.* (2000).

4. Slender-drop approximation

Considerable insight into this type of extensional flow can be obtained through an approximate one-dimensional slender-drop analysis which is not subject to numerical inaccuracy arising from a deforming mesh as in the above finite-element computations. The following development in the main relates to three-dimensional drops where the drop length is much greater than any cross-section area; however, it also applies to two-dimensional sheets where the length is much greater than the sheet thickness.

In a Lagrangian reference frame (Wilson 1988; Stokes *et al.* 2000) we let $x = X(\xi, t)$, where ξ is a fluid-particle label such that $x = \xi$ at $t = 0$. The initial drop geometry is assumed to have a cross-section area distribution given by some function $A_0(\xi)$. That is, $A(\xi, 0) = A_0(\xi)$, $0 \leqslant \xi \leqslant L_0$, where $A(\xi, t)$ is the cross-sectional area at label ξ and time t, and L_0 is the initial drop length.

Consider a small element located at $\xi = \xi_1$, with length $\mathrm{d}x = X_\xi(\xi_1, t)\,\mathrm{d}\xi_1$ and volume $\mathrm{d}V = A(\xi_1, t)\,\mathrm{d}x$. Conservation of mass demands that $\mathrm{d}V$ is time-independent, i.e. $A(\xi_1, t)\,\mathrm{d}x = A_0(\xi_1)\,\mathrm{d}\xi_1$. Since $\mathrm{d}x = X_\xi\,\mathrm{d}\xi_1$, we have

$$A\frac{\partial X}{\partial \xi} = A_0\ , \tag{4.1}$$

which is the differential form of the Lagrangian continuity equation. Integration from the wall to a general ξ yields

$$X(\xi, t) = \int_0^\xi \frac{A_0(\xi_1)}{A(\xi_1, t)}\,\mathrm{d}\xi_1 \tag{4.2}$$

as in Stokes *et al.* (2000).

Newton's second law for this element states that its mass multiplied by its downward acceleration is equal to its weight less the net viscous force resisting elongation. The latter viscous force can be written as stress σ multiplied by area A on the top side $\xi = \xi_1$ minus that on the bottom side $\xi = \xi_1 + \mathrm{d}\xi_1$. Thus, if $a = a(\xi_1, t) = X_{tt}(\xi_1, t)$ is the downward acceleration,

$$(\rho \mathrm{d}V)a = (\rho \mathrm{d}V)g + \Big[\sigma A\Big]_{\xi=\xi_1}^{\xi=\xi_1+\mathrm{d}\xi_1}\ . \tag{4.3}$$

Using the continuity requirement $\mathrm{d}V = A\mathrm{d}x = A_0\mathrm{d}\xi_1$ as above, and summing over all elements $\xi = \xi_1$ lying below station ξ, assuming zero stress $\sigma = 0$ at the bottom $\xi = L_0$ of the drop, we have

$$\int_{\xi}^{L_0} \rho\,[g - a(\xi_1, t)]\,A_0(\xi_1)\,\mathrm{d}\xi_1 = \sigma(\xi, t)A(\xi, t) = -\mu^* \frac{\partial}{\partial t} A(\xi, t). \tag{4.4}$$

In the above, $\mu^* = 3\mu$ is the elongational (Trouton) viscosity (Bird *et al.* 1977, p. 30), which relates stress σ and elongational rate of strain $-A_t/A$. Integrating (4.4) with respect to time t gives

$$A(\xi, t) = A_0(\xi) - \frac{\rho}{\mu^*} \int_{\xi}^{L_0} A_0(\xi_1)\,[gt - u(\xi_1, t)]\,\mathrm{d}\xi_1, \tag{4.5}$$

where $u(\xi_1, t) = X_t(\xi_1, t)$ is the downward velocity of the element at $\xi = \xi_1$.

Equation (4.5) is the appropriate generalization of the corresponding inertialess equation in Stokes *et al.* (2000), namely that resulting from dropping the term in u, and is to be solved together with the continuity equation (4.2).

Equivalent Eulerian equations are also not difficult to construct. Defining a small slenderness parameter (in three dimensions) as the maximum value of $\sqrt{A_0(x)}/L_0$, a formal asymptotic expansion of (2.1) and (2.2) with respect to this parameter yields equations for the Eulerian velocity $u(x, t)$ and cross-section area $A(x, t)$, namely a 'one-dimensional Navier–Stokes equation'

$$\frac{\partial u}{\partial t} + u\frac{\partial u}{\partial x} = g + \nu^* \frac{1}{A}\frac{\partial}{\partial x}\left(A\frac{\partial u}{\partial x}\right) \tag{4.6}$$

($\nu^* = \mu^*/\rho$), and a one-dimensional continuity equation

$$\frac{\partial A}{\partial t} + \frac{\partial}{\partial x}(Au) = 0\,. \tag{4.7}$$

Equations equivalent to (4.6) and (4.7) were given by Kaye (1991). In practice, the Lagrangian system (4.5) and (4.2) is much easier to solve. However, the presence of the term in $u = X_t$ in (4.5) couples the two Lagrangian equations and variables X and A together, which means that the Lagrangian solution is no longer explicit as a pair of quadratures, as it was in Stokes *et al.* (2000).

4.1. *Nonlinear diffusion equations*

We proceed by differentiating (4.5) with respect to ξ, dividing through by $A_0(\xi)$, and then differentiating again with respect to ξ to give

$$\frac{\partial}{\partial \xi}\left[\frac{1}{A_0}\frac{\partial}{\partial \xi}(A - A_0)\right] = -\frac{1}{\nu^*}\frac{\partial u}{\partial \xi}. \tag{4.8}$$

Differentiating (4.2) with respect to t and ξ gives u_ξ in terms of A, and substituting into (4.8) finally yields

$$\frac{\partial A}{\partial t} = \nu^* \frac{A^2}{A_0}\frac{\partial}{\partial \xi}\left[\frac{1}{A_0}\frac{\partial}{\partial \xi}(A - A_0)\right]\,. \tag{4.9}$$

For any given initial drop shape $A_0(\xi)$, we must solve the partial differential equation (4.9) for $A(\xi, t)$ subject to the initial condition

$$A(\xi, 0) = A_0(\xi)\,. \tag{4.10}$$

The boundary condition at the bottom (free) end of the drop $\xi = L_0$ is just

$$A(L_0, t) = A_0(L_0)\,, \tag{4.11}$$

obtained by setting $\xi = L_0$ in (4.5) and equivalent to the Eulerian zero-stress condition $u_x = 0$. The zero normal-velocity boundary condition $u = 0$ at the wall end $\xi = 0$ is

$$\frac{\partial A}{\partial \xi}(0, t) = A_0'(0) + \frac{g}{\nu^*} A_0(0) t, \tag{4.12}$$

obtained by differentiating (4.5) with respect to ξ and setting $\xi = 0$. The zero tangential-velocity boundary condition at the wall is by necessity violated in this slender-drop approximation; when included, it induces a wall boundary layer, as discussed in Stokes *et al.* (2000). Once $A(\xi, t)$ is found, we use the continuity equation (4.2) to find $X(\xi, t)$, and hence the drop length $L(t) = X(L_0, t)$.

A suitable non-dimensional form of this problem follows by scaling $A(\xi, t)$ and $A_0(\xi)$ with respect to $A_0(0)$, ξ with respect to L_0, and t with respect to $\nu^*/(gL_0)$. Then equation (4.9) becomes

$$\frac{A^2}{A_0} \frac{\partial}{\partial \xi} \left[\frac{1}{A_0} \frac{\partial (A - A_0)}{\partial \xi} \right] = Re \frac{\partial A}{\partial t}\,, \tag{4.13}$$

where Re is defined by equation (2.3). Equation (4.13) is a nonlinear diffusion equation, with a diffusivity proportional to the square of the 'concentration' A. In the special case $A_0 = 1$, this equation was derived by Kaye (1991, equation (4.3.20), p. 72) from an Eulerian formulation. Although for this special case $A_0 = 1$, there are methods (see e.g. Ames 1972, p.14) for converting (4.13) to a linear diffusion equation, and hence solving analytically, these solutions are not appropriate for the present boundary conditions or for more general initial shapes, and we shall instead use direct numerical methods.

The inertialess limit is $Re = 0$, and in that limit, the explicit solution of (4.13) subject to the scaled boundary and initial conditions is

$$A(\xi, t) = A_0(\xi) - t \int_{\xi}^{1} A_0(\xi_1)\, \mathrm{d}\xi_1 \tag{4.14}$$

which is just a scaled version of (4.5), with the inertia term in u dropped. Thus, for the initially paraboloidal drop $A_0 = 1 - \xi$, we have

$$A(\xi, t) = 1 - \xi - \frac{t}{2}(1 - \xi)^2\,, \tag{4.15}$$

corresponding (via (4.2) with $\xi = 1$) to a drop length

$$L(t) = -\frac{2}{t} \log \left[1 - \frac{t}{2} \right], \tag{4.16}$$

which becomes infinite at the (scaled) crisis time $t = 2$. However, we expect that for any finite Re, the drop length remains finite for all finite t, and that for large t, the acceleration approaches gravity, which means that $ReL''(t) \to 1$. The cross-section area at this crisis time is $A(\xi, 2) = \xi(1 - \xi)$ when $Re = 0$. We shall observe later that this is also the large-t limit of the solution for arbitrary Re.

4.2. *Slender-drop numerical computations*

In the general case, it is convenient to define $B(\xi, t) = A(\xi, t) - A_0(\xi)$ as the departure from the initial shape $A_0(\xi)$. Then, (4.13) is a nonlinear diffusion equation for B, with diffusivity proportional to $A^2 = (A_0 + B)^2$.

We have for the present purpose solved (4.13) numerically, and indeed have not found it necessary to use anything other than the most direct explicit finite-difference method, i.e. with time step Δt and space step $\Delta\xi$, we approximate (4.13) by

$$B(\xi, t+\Delta t) = B(\xi, t) + D\left[\frac{B(\xi+\Delta\xi, t) - B(\xi, t)}{A_0(\xi+\Delta\xi/2)} - \frac{B(\xi, t) - B(\xi-\Delta\xi, t)}{A_0(\xi-\Delta\xi/2)}\right], \quad (4.17)$$

where

$$D = \frac{\Delta t A(\xi, t)^2}{Re\Delta\xi^2 A_0(\xi)}. \quad (4.18)$$

The boundary conditions are $B = 0$ at $t = 0$ and $\xi = 1$, and $\partial B/\partial\xi = t$ at $\xi = 0$; the latter is implemented simply by defining an artificial value $B(-\Delta\xi, t) = B(\Delta\xi, t) - 2t\Delta\xi$ for use in the last term of (4.17) at $\xi = 0$.

The diffusion number D must be kept less than 0.5 for numerical stability, which presents no problems with respect to nonlinearity since the cross-section area $A = A_0 + B$ tends to reduce from its initial value, but does present a few problems when Re is small, which is of course the most interesting case. In practice, however, there appear to be no barriers to use of extremely small time steps Δt when Re is small. We have generally found that $\Delta\xi \approx 0.02$ gives adequate spatial accuracy; but then, for example, with $Re = 0.001$ we need a time interval $\Delta t \approx 10^{-7}$ for stability.

The actual results for $A(\xi, t)$ are simple and well behaved. The cross-section area at first reduces steadily and almost linearly with respect to time t, as in the inertial-less limit (4.14). Near the crisis time ($t = 2$ for the initially paraboloidal case) and for particles near $\xi = 0$ (i.e. initially close to the wall), the rate of this reduction in area slows down and then A slowly approaches zero at $\xi = 0$ as time further increases, suggesting break-off at the wall.

It appears from our computations for $A_0 = 1-\xi$, shown in figure 5, that $A(\xi, t) \to \xi(1-\xi)$ as $t \to \infty$, in agreement with a large-time asymptotic theory to be discussed below (figure 6). Kaye (1991) conjectured (based on results from a relatively coarse discretization for $A_0 = 1$) that the wall value of A would become negative at a finite time t identifiable as that for breaking. However, we have found no such tendency in our computations for any initial shape $A_0(\xi)$, and believe that breaking cannot occur in the present model (which neglects surface tension) for any $Re > 0$, and that A must formally remain non-negative for ever.

There is good comparison between the slender-drop results shown in figure 5 and our earlier finite-element results shown in figure 3. Noting that the main drop shape below the filament given by our finite-element computations appears to approach

$$A = \frac{(\xi - 0.7\alpha_r)}{(1 - 0.7\alpha_r)}(1-\xi) \quad (4.19)$$

as $t \to \infty$, we retrieve the slender-drop result $A \to \xi(1-\xi)$ as $\alpha_r \to 0$. The pinching of the filament seen in finite-element simulations at $\xi \approx \alpha_r$ will not be observable in the slender-drop limit, but can perhaps be associated with the large slope $\partial A/\partial\xi$ that develops at large time at $\xi = 0$, as indicated by (4.12). It is tempting to attribute the differences seen between figures 3 and 5 solely to the fact that slip is necessarily permitted along the wall in the slender-drop theory which is not permitted in finite-element simulations. Certainly, this results in a wall boundary layer in figure 3 which is absent in figure 5. However, this does not explain the pinching of the filament just above the main drop.

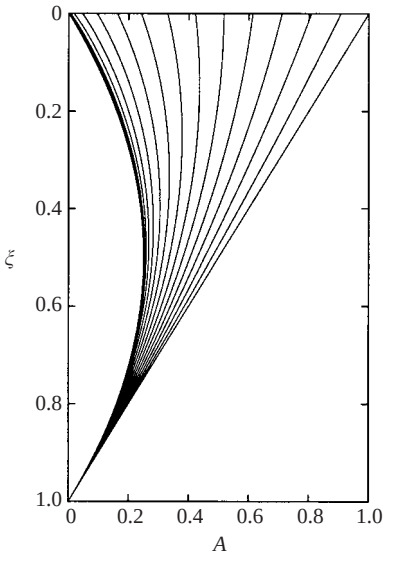

FIGURE 5. Drop cross-section area A as a function of initial distance from the wall ξ, for the initially paraboloidal drop at Reynolds number $Re = 0.1$, for times $t = 0, 0.2, 0.4, \ldots, 3.6$. Computed using the slender-drop theory. The drop shape progressively changes from initially paraboloidal $A = 1 - \xi$ to a final profile $A = \xi(1 - \xi)$.

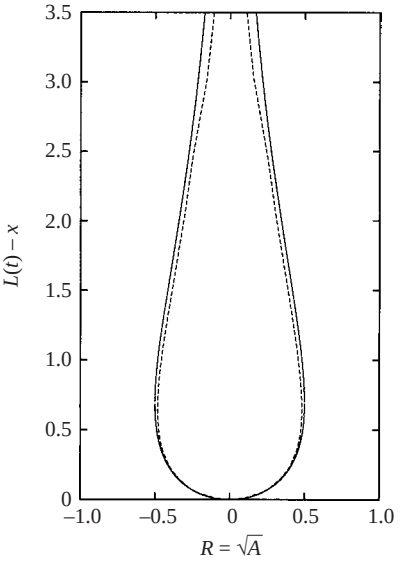

FIGURE 6. Drop radius as a function of $L(t) - x$ at large time t for the initially paraboloidal drop, $\alpha_r = 0.1$, $Re = 0.1$. —, large-time asymptotic equation (4.26) and slender-drop theory which are indistinguishable, ---, finite-element computation with no-slip wall boundary at $t = 4$.

This is emphasized by repeating the finite-element simulation, but now with the condition of zero tangential velocity along the wall boundary replaced by zero tangential stress; this allows slip along the wall similar to that permitted by the slender-drop theory. Plotting A versus ξ at different times yields curves practically

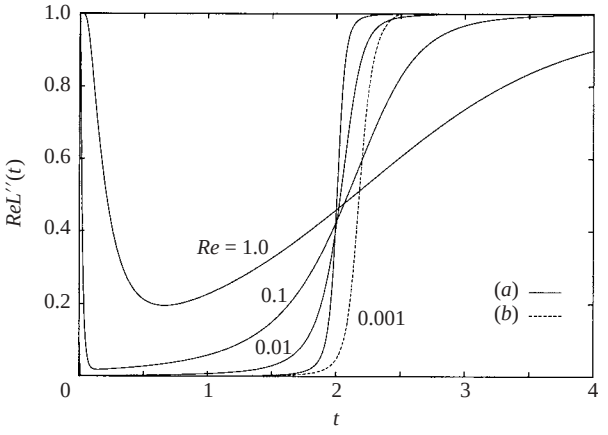

FIGURE 7. Acceleration $ReL''(t)$ versus time t for an initially paraboloidal slender drop. (a) Slender drop theory and (b) finite-element curve for $Re = 0.001$, $\alpha_r = 0.1$.

identical to those in figure 5, excepting for a small deviation near the wall. In particular, at large time $A \to \xi(1-\xi)$, but there is pinching of the drop quite similar to that seen in figure 3, albeit now near $\xi = \alpha_r/2$ (not $\xi \approx \alpha_r$). This translational shift is a consequence of the no-slip boundary layer of thickness $O(\alpha_r/2)$, which does not develop in the case of a slip boundary. The pinching, however, appears to be related to the fact that with either a no-slip or slip wall boundary, the slope $\partial A/\partial\xi$ must become zero at some point above the main drop (at the wall in the latter case). This is not permitted by the slender-drop theory for the initially paraboloidal drop under investigation which demands $\partial A/\partial\xi(0,t) > 0$ for all time.

Returning to our slender-drop theory, once we have solved for $A(\xi,t)$, other flow variables follow, in particular, the acceleration as measured by the second time derivative of the drop length. This is computed from $A(\xi,t)$ by evaluating the velocity $u(\xi,t)$ by numerical ξ-differentiation of (4.5), followed by numerical t-differentiation of the bottom velocity $u(1,t) = L'(t)$. In figure 7, we plot $ReL''(t)$ versus time for various values of Re, for an initially paraboloidal slender drop. As with the finite-element results, this quantity starts and ends at 1, with a viscosity-dominated time period of low accelerations in between. As before, reducing Re causes the rise in acceleration near $t = 2$ to become steeper and steeper and to approach closer and closer to the inertialess crisis at $t = 2$. The curves from the finite-element computations for an initially paraboloidal drop of aspect ratio $\alpha_r = 0.1$ (see figure 1), compare well with their slender-drop theory counterparts. The exact computations display a time delay relative to the slender-drop computations in the return to acceleration due to gravity, shown in figure 7 for $Re = 0.001$. This is attributable to the effect of the no-slip wall boundary, and decreases as the aspect ratio decreases.

Of even more interest is the acceleration profile in the drop, as a function of ξ, in the slender-drop limit. This is shown over a range of times in figure 8. As in the finite-element calculations we find that, after a relatively short time, the acceleration takes its maximum value at a position in the interior of the drop for a considerable time, with this position moving towards the wall as time progresses. However, the maximum acceleration is very much larger than in the finite-element computations and, because of limitations on the spatial grid near $\xi = 0$, we have not been able to determine just how large it becomes, but only that it increases as our grid resolution

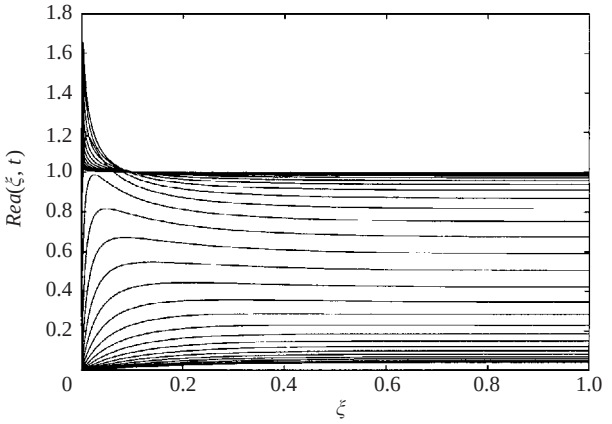

FIGURE 8. Acceleration as a function of initial position ξ for the initially paraboloidal drop in the slender drop limit, $Re = 0.1$, $t = 0.8, 0.9, \ldots, 3.9$.

at the wall increases. Further, the position of maximum acceleration appears to approach the wall, whereas in our finite-element computations it only came as close as $\xi \approx \alpha_r$ which we identify as the transition region between the main drop and the filament.

At large time, in the slender-drop limit, the acceleration versus ξ curve appears to approach the step function $Re\,a(\xi, t) = 1$, $1 \leqslant \xi < 0$, $Re\,a(0, t) = 0$ as $t \to \infty$, as seen in figure 8, with no progressive decrease in acceleration from g at $\xi = \alpha_r$ to 0 at $\xi = 0$, as occurred in the finite-element computations. This seems to be associated with the fact that pinching of the connecting filament occurs at $\xi = 0$ in the slender-drop limit, with the whole of the drop effectively going into free fall, and implies that the drop will break (owing to surface tension) at the wall.

The actual axisymmetric drop shapes in the physical plane are shown in figure 9(*a*) by plotting the (longitudinally-scaled) length coordinate $x = X(\xi, t)$ versus the (laterally-scaled) scaled radius co-ordinate $R = \sqrt{A(\xi, t)}$. The equivalent curves from the finite-element computations are shown, for comparison in figure 9(*b*). This time history seems quite sensible, and in particular demonstrates for large time an approach to a freely falling state which we now discuss. Note that the vertical scale is the initial drop length L_0 whereas the horizontal scale is the initial maximum drop radius $R_0(0)$; to provide a faithful picture of actual slender drops, these and all figures in this paper would need to be considerably stretched vertically, and for example the final drop appearance would have a more rounded bottom.

4.3. *Large-time drop shape*

An intuitive argument for the large-time behaviour is as follows, reverting temporarily to unscaled variables.

Once the drop is in free fall as if it were a rigid body, its velocity must be of the form

$$u(\xi, t) = g(t - t_0) \tag{4.20}$$

for some constant t_0, physically interpretable as the apparent time when this free fall begins. Because of the initial slowing down of motion owing to viscosity, we expect that $t_0 > 0$, but otherwise, in principle, the quantity t_0 is unknown in advance.

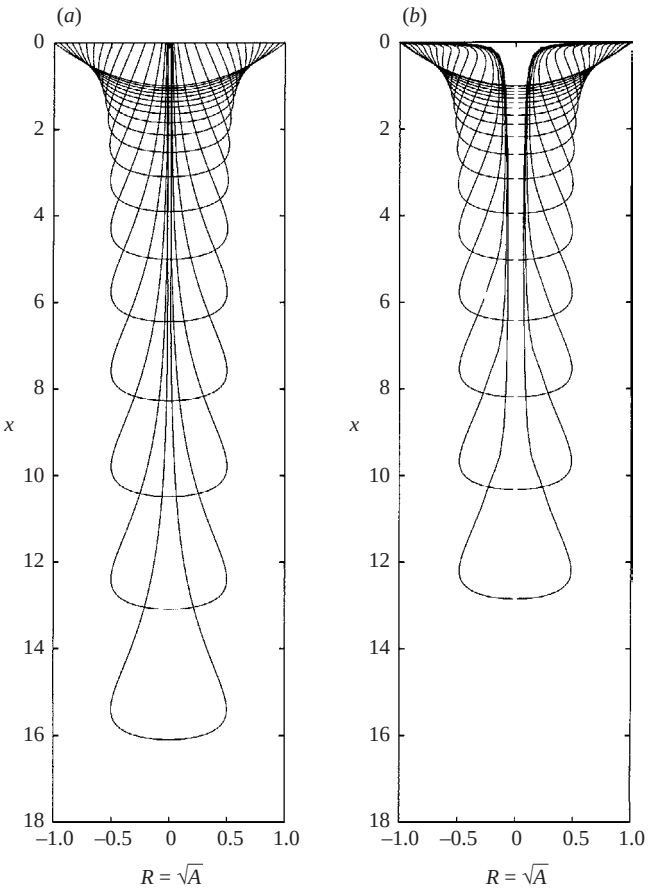

FIGURE 9. Evolution of the initially paraboloidal drop, as seen in physical coordinates x, R. (a) Slender-drop theory, (b) finite element simulation. $Re = 0.1$, $t = 0, 0.2, 0.4, \ldots, 3.6$.

However, when fluid inertia has only a small effect, i.e. for relatively small Re, we may expect that $t_0 = t^*$, where t^* is the crisis time (when formally the inertialess theory of Stokes *et al.* (2000) predicts breaking), because then close to the crisis time, the acceleration of the drop (excepting a small region near the wall) rapidly approaches g and remains at that value thereafter. Prior to this event, all fluid velocities $u(\xi, t)$ were small, and from a large-t viewpoint we may assume that the drop was then at rest.

If we substitute (4.20) into (4.5), we find

$$A(\xi, t) = A_0(\xi) - \frac{g}{\nu^*} t_0 V(\xi) \tag{4.21}$$

where

$$V(\xi) = \int_{\xi}^{L_0} A_0(\xi_1)\, \mathrm{d}\xi_1 \tag{4.22}$$

is the volume of drop fluid below station ξ. The fact that this asymptotic shape function $A(\xi, t)$ is actually independent of time t confirms the final rigid-body character of the freely falling drop.

Now in the present slender-drop theory, there is slip at the wall, and for a large family of initial drop shapes, including those considered above, it appears that the drop diameter at the wall tends to zero at large times. If therefore we demand in (4.21) that $A = 0$ at $\xi = 0$, we find

$$t_0 = \frac{\nu^*}{g}\frac{A_0(0)}{V(0)} \tag{4.23}$$

so

$$A(\xi, t) = A_0(\xi) - \frac{A_0(0)}{V(0)}V(\xi)\ . \tag{4.24}$$

It happens that (4.23) is the correct formula for the crisis time t^* in the inertialess theory of Stokes *et al.* (2000), for those initial drops that break at the wall according to that theory, confirming that $t_0 \approx t^*$ when *Re* is small.

Indeed, we expect that $t_0 \approx t^*$ in all cases, whether or not inertia is small, and whether or not the drop breaks at the wall, but this is not yet proved. In any case, there appears to be a remarkable relationship between the inertialess theory and the large-time limit of the flow with inertia. Namely, as $t \to \infty$ in a computation including inertia, the drop shape approaches that which would have been obtained at the (finite) crisis time $t = t^*$ in a computation neglecting inertia. Specifically, for the initially paraboloidal drop $A_0 = 1-\xi$, with $V(\xi) = (1-\xi)^2/2$, we have $A \to \xi(1-\xi)$, and this is confirmed by our computations.

The actual final drop shape as a function of the physical coordinate $x = X(\xi, t)$ is obtained by integrating the continuity equation (4.1). However, this integration cannot be (as with (4.2)) from the wall $\xi = 0$, where (4.24) has $A = 0$, because this integral diverges. Of course it must so diverge, since at infinite times the drop is an infinite distance from the wall. If instead we integrate from the bottom $\xi = L_0$ of the drop, using the asymptotic estimate (4.24) for $A(\xi, t)$, we find

$$X(\xi, t) = L(t) - \int_{\xi}^{L_0} \frac{A_0(\xi_1)\,\mathrm{d}\xi_1}{A_0(\xi_1) - [A_0(0)/V(0)]V(\xi_1)}\ . \tag{4.25}$$

Equations (4.24) and (4.25) provide the formal connection between initial and final drop shapes.

For example, the initially paraboloidal drop with $A_0 = 1-\xi$ gives $X = L(t) + \log\xi$, or $\xi = \mathrm{e}^{-(L-x)}$. Thus, the asymptotic radius of this family of drops is $R(x) = \sqrt{A}$, where

$$A = \mathrm{e}^{-(L-x)}[1 - \mathrm{e}^{-(L-x)}]\ , \tag{4.26}$$

which is an explicit function of distance $L(t)-x$ measured upward from the bottom of the drop, and agrees closely with the computed large-time drop shape obtained from the slender-drop theory and our finite-element computations, as shown in figure 6. This final drop has maximum diameter equal to 0.5 (times the original maximum diameter) at a distance $\log 2 = 0.693$ (times the original length) above the bottom, and its thickness then decays exponentially at greater distances above the bottom.

The present asymptotic theory does not quite provide an estimate of the actual bottom position $x = L(t)$, although equation (4.20) gives an estimate of its time derivative $L'(t) = u(L_0, t)$. Further work would be needed to estimate the constant of integration, i.e. the apparent initial length $L(t_0) = L(t) - g(t-t_0)^2/2$.

In summary, the asymptotic theory of the present section enables explicit estimates of the shape of the drop in its 'final' freely falling rigid-body-like state, given any initial shape. There must also be a thin filament connecting this drop to the wall,

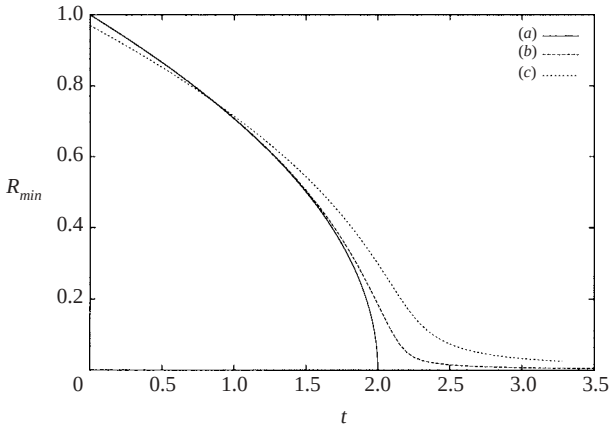

FIGURE 10. Radius R_{min} versus time t of the point in the filament which becomes the point of minimum radius. (a) inertialess slender-drop theory, (b) slender-drop theory with inertia, $Re = 0.01$, (c) exact finite-element computation, $Re = 0.01$, $\alpha_r = 0.1$.

whose thickness reduces with time. The above description applies until surface tension breaks the filament, and eventually (after a sufficient time in free fall) converts any three-dimensional drop into a sphere.

5. The filament

Confining attention to those drops which break at the wall according to the inertialess slender-drop theory of Stokes *et al.* (2000), namely those initial drop shapes with $V(\xi)/A_0(\xi)$ monotone decreasing, the filament region is that for small ξ ($< \alpha_r$), and the filament consists therefore only of particles that were originally close to the wall. It is a very difficult computational task to retain accurate representations of the solution in such a small region while simultaneously representing the main drop for all finite values of ξ, and hence we cannot expect either the finite-element or slender-drop computations to capture accurately the fine details of the filament shape. Nevertheless, we believe that some qualitative understanding may be obtained by an examination of our results.

It is of interest to consider the decrease in radius over time of the point along the drop axis which becomes the point of minimum radius in the filament. For the slender-drop theory this point is at the wall, but for the exact problem it is initially a little below the wall. Curves from the slender-drop-theory and finite-element computations, for a small Reynolds number $Re = 0.01$, are shown in figure 10 (curves (b) and (c), respectively) and are in reasonable agreement, with this agreement improving as $\alpha_r \to 0$ in the exact problem. The inertialess slender-drop theory of Stokes *et al.* (2000) predicts a minimum radius R_{min} (scaled with $R_0(0)$) given by

$$R_{min} = \left(\frac{t^* - t}{t^*}\right)^{1/2}, \qquad t^* = 2, \tag{5.1}$$

where t is time, scaled with $\nu^*/(gL_0)$ as earlier. This curve is also shown (as curve (a)) in figure 10, from which we see that the present theory including inertia yields curves agreeing with (5.1) for a considerable time, but then deviating from it near to the crisis time $t = 2$ of the inertialess slender-drop theory. This behaviour is as expected since, as commented earlier, with the current theory neglecting surface tension, the

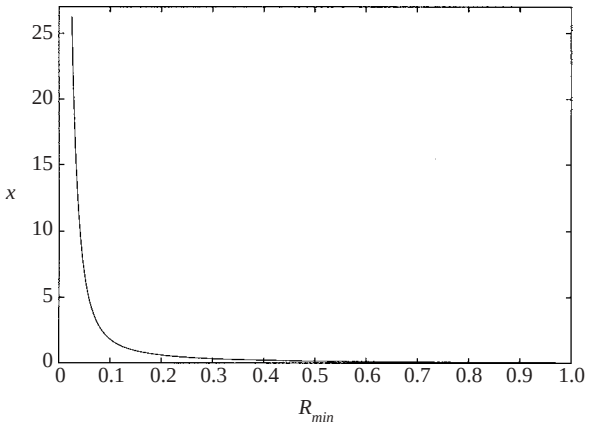

FIGURE 11. Distance below the wall x versus radius R_{min} of the point in the filament which becomes the point of minimum radius. Exact finite-element computations, $Re = 0.01$, $\alpha_r = 0.1$.

drop does not formally break. The agreement with (5.1) increases as $Re \to 0$, which is also according to expectation.

Comparisons of finite-element computations for drops of finite radius with results from the slender-drop theory do show some interesting differences in the apparent filament behaviour, which is most clearly evident from figures 9(*a*) and 9(*b*). Specifically, the radial dimension in the transition region between the main drop and filament, that is about three initial drop lengths above the bottom of the main drop, is smaller for the computations for drops of finite radius than those for drops in the slender limit. Then, the computations for drops of finite radius show a somewhat cylindrical filament above this region (figure 9*b*) compared with the upward monotonically decaying filament radius of the slender-drop limit (figure 9*a*).

Note that because the filament is so long, even though it consists only of particles that were originally close to the wall, the actual break point along the filament could be quite far from the wall. Indeed, for drops of finite radius, our finite-element computations suggest that this is the case, with the distance from the wall of the point of minimum radius, where eventual break-off due to surface tension can be expected, increasing rapidly as the radius decreases over time. This is shown in figure 11. It is not clear whether the distance from the wall becomes infinite or approaches some large finite value as $R_{min} \to 0$. Applying the inertialess theory (Stokes *et al.* 2000) in the filament region, which seems reasonable, would lead to the conclusion that $x \to \infty$ as $R_{min} \to 0$ but, in any case, the physical distance along the filament certainly becomes very large.

It is worth commenting that, while the slender-drop theory predicts breaking 'at' the wall and the exact theory predicts breaking 'near' the wall in Lagrangian space which could physically mean a long way from the wall, both theories predict very similar time histories for the minimum radius, as already seen in figure 10. The agreement with the inertialess slender-drop result (5.1), indicates that the minimum filament radius decreases like the time distance from breakup to the half power, up until times quite near to breakup. Near to breakup, analyses including surface tension, but in the absence of gravitational pull, typically give (Eggers 1997)

$$R_{min} \sim (t^* - t)^{\beta},$$

and it has been shown (Renardy 1995; Renardy & Losh 2002) that, for very viscous fluids, β may take a value between 1/2 and 1 depending on the initial stretch conditions, with $\beta = 1$ if it is assumed that viscous and surface tension forces contribute at the same order. However, where gravitational pull is responsible for filament stretching, very thin threads can persist well beyond time scales indicated by current theories and a quantitative explanation of this is still lacking (Eggers 1997).

Any further meaningful analysis of the ultimate behaviour of these very thin filaments must include surface tension. We can expect that surface tension will play a significant role when and where lateral length scales are comparable with the meniscus size, and that surface tension will finally determine the exact breaking position.

6. Conclusion

By including inertia terms in the flow model, both in a slender-drop approximation and in an exact computation, we have demonstrated how, in both the very early and very late stages of the fall of a drop of viscous fluid, the drop's acceleration becomes equal to the acceleration due to gravity g. In the intervening period, from soon after it begins its descent until a 'crisis' time when a rapid increase occurs, accelerations are small compared to gravity, and neglect of inertia is valid for small values of the parameter $Re = gL_0^3/\nu^{*2}$. The crisis time $t^* = O(\nu^*/(gL_0))$ computed from the inertialess theory is then a good estimate of the time at which the drop acceleration increases rapidly toward g, when we can expect the drop to break and go into free fall.

Drop shapes are available from the exact or slender-drop computations at all times and for all Reynolds numbers. However, the slender-drop theory also provides explicit formulae via simple quadratures for the final quasi-rigid-body shape of the drop when it is in free fall prior to smoothing by surface tension, this shape being the same as the inertialess theory predicts at the finite crisis time.

Including inertia may also provide insight into the behaviour of the ever-thinning filament which connects this ultimate drop to the wall, prior to breaking events controlled by surface tension. This, however, must be confirmed by an analysis that includes surface tension.

This work was supported by the Australian Research Council through a Post-doctoral Fellowship to Y. M. S. and a grant to E. O. T. The authors acknowledge valuable discussions with Professor P. Broadbridge and Professor L. W. Schwartz. Thanks also to the referees whose comments resulted in a much improved paper.

REFERENCES

Ames, W. F. 1972 *Nonlinear Partial Differential Equations in Engineering*. Interscience.

Barnichon, J. D., Havenith, H., Hoffer, B., Charlier, R., Jongmans, D. & Duchesne, J. C. 1999 The deformation of the Egersund-Ogna anorthosite massif, south Norway: finite-element modelling of diapirism. *Tectonophysics* **303**, 109–130.

Bird, R. B., Curtiss, C. F., Armstrong, R. C. & Hassager, O. 1977 *Dynamics of Polymeric Liquids, vol. 1 Fluid Mechanics*. Wiley.

Cram, L. E. 1984 A numerical model of droplet formation. In *Computational Techniques and Applications: CTAC-83* (ed. J. Noye & C. Fletcher), pp. 182–188. Elsevier.

CSIRO 1999 *Fastflo version 3, Tutorial Guide*. Commonwealth Scientific and Industrial Research Organisation (CSIRO). Australia.

Eggers, J. 1993 Universal pinching of 3D axisymmetric free surface flow. *Phys. Rev. Lett.* **71**, 3458–3460.

Eggers, J. 1997 Nonlinear dynamics and breakup of free surface flows. *Rev. Mod. Physics* **69**, 865–929.

Gearing, D. R. 1999 Apparatus and method for improved optical glass GOB preform production. United States Patent 5 900 033.

Haidar, J. & Lowke, J. J. 1996 Predictions of metal droplet formation in arc welding. *J. Phys.* D: *Appl. Phys.* **29**, 2951–2960.

Henderson, D., Segur, H., Smolka, L. B. & Wadati, M. 2000 The motion of a falling liquid filament. *Phys. Fluids* **12**, 550–565.

Kary, J., Eggles, F., Imschweiler, D. & Zerbe, D. 2000 Corning Asahi Video Products (CAV). Fall 2000 Industry Project, Penn State University. See www.me.psu.edu/me4/fall00/corning1/

Kaye, A. 1991 Convected coordinates and elongational flow. *J. Non-Newtonian Fluid Mech.* **40**, 55–77.

Papageorgiou, D. T. 1995 On the breakup of viscous liquid threads. *Phys. Fluids* **7**, 1529–1544.

Renardy, M. 1995 A numerical study of the asymptotic evolution and breakup of Newtonian and viscoelastic jets. *J. Non-Newtonian Fluid Mech.* **59**, 267–282.

Renardy, M. & Losh, D. 2002 Similarity solutions for jet breakup in a Giesekus fluid with inertia. *J. Non-Newtonian Fluid Mech.* **106**, 17–27.

Sarkar, K. & Schowalter, W. R. 2001 Deformation of a two-dimensional drop at non-zero Reynolds number in time-periodic extensional flows: numerical simulation. *J. Fluid Mech.* **436**, 177–206.

Stokes, Y. M., Tuck, E. O. & Schwartz, L. W. 2000 Extensional fall of a very viscous fluid drop. *Q. J. Mech. Appl. Maths* **53**, 565–582.

Wilkes, E. D., Phillips, S. D. & Basaran, O. A. 1999 Computational and experimental analysis of dynamics of drop formation. *Phys. Fluids* **11**, 3577–3598.

Wilson, S. D. R. 1988 The slow dripping of a viscous fluid. *J. Fluid Mech.* **190**, 561–570.